This is a peer-reviewed, accepted author manuscript of the following research article: Zaman, T, Syed, M, Feng, Z & Burt, G 2024, 'A realigned instantaneous frequency approach for SSCI oscillation localization in power networks', IEEE Transactions on Power Systems. https://doi.org/10.1109/TPWRS.2024.3474177

A Realigned Instantaneous Frequency Approach for SSCI Oscillation Localization in Power Networks

Taimur Zaman, Mazheruddin Syed, Zhiwang Feng, and Graeme Burt

***Abstract*—The detection and localization of the grid oscillations stemming from subsynchronous control interactions (SSCI) presents notable challenges. These include the limited reporting rate of Phasor Measurement Units, spectral leakage, and picket fence effects, which inadvertently misreport the amplitude and frequency of modes constituting these complex oscillations. To accurately detect the oscillations and localize the participating sources, a systematic approach employing synchro-waveforms is proposed. Firstly, the modes of oscillations are extracted using a time-frequency transformation, where, a realigned instantaneous frequency-based synchro transform is developed to address noise and time-varying constraints. This is further improved by employing an adaptive window which improves the energy concentration to retain the reconstruction of modes for strongly time-varying signals with significant noise. A decoupled admittance model is then extracted from the modes obtained at varying operating conditions. Consequently, a global admittance matrix is constructed identifying the active/reactive source of complex oscillation in the network. The efficacy and robustness of the proposed method against the state-of-the-art are proven by employing numerical simulations on sample networks and real-world data obtained from networks experiencing SSCI oscillations.**

***Index Terms*—Subsynchronous control interaction (SSCI), Realigned instantaneous frequency (IF), Oscillation detection and source localization, Synchro transform.**

I. Introduction

THE integration of solar and wind energy into power grids is essential to ensure the transition to net-zero at pace [1]. The seamless integration of these energy sources into the grid necessitates the incorporation of modern power converter topology and advanced control mechanisms. As a result, the dominance of power converters in power systems is increasing, examples of such technologies include double-fed induction generators (DFIGs), high voltage DC (HVDC) systems, and flexible AC transmission (FACTs) devices. However, this shift towards inverter-based resources (IBRs) introduces notable challenges in reliable and secure operation of the power system. The control of interconnected power converters can incite resonances and control-based interactions with other components of the power system [2], and can result in escalating power oscillations [3].

Unlike low-frequency oscillations or torsional oscillations in conventional wind power systems, recent studies show that complex electromagnetic oscillations in weak grids emerge due to sub-synchronous control interactions (SSCI) between components of the weak grid and control of IBRs [3]. The phenomenon is demonstrated by incidents reported in the last decade [4], emerging primarily due to the employment of phase-locked loop (PLL) and d-q transformation-based IBR control [5], resulting in complex sub- and/or super-synchronous oscillations [6], [7]. Examples of such incidents are widely reported in power networks around the world, examples include Hami [7], ERCOT [8], and Guyuan [9] networks.

Corresponding authors: Taimur Zaman; Zhiwang Feng.

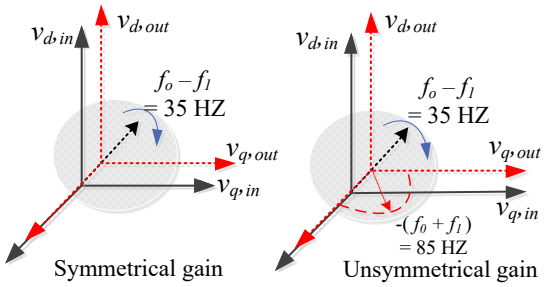

Fig. 1: dq transformation and coupling frequency effect due to (a) symmetrical gains, (b) unsymmetrical gains.

When an IBR with PLL for control and grid synchronization experiences a disturbance with Inter-harmonic Frequency (IhF), subsequent effect in terms of coupled frequencies can be observed in the output [10] as shown in Fig. 1. For balanced grid and symmetrical gains of PLL as shown in Fig. 1a, the IhF with 15 Hz component in the dq rotating frame will appear as 35 Hz component at the control input. Similarly, for unsymmetrical gains and unbalanced grid conditions, an additional coupled frequency appears at the control inputs of current loops as a result of voltage perturbation by IhF [11]. To make it simple, the interpolation of these coupled frequency-based modes (sub-synchronous (subSR) and super-synchronous (supSR)) into fundamental frequency interacts with other network components and emerges as complex and multi-mode synchronous resonance (MSR) based oscillations in the network [12]. Therefore, the theoretical bounds suggest a potential increase in the complexity of the phenomena for networks dominated by IBRs, significantly impacting the PCC impedance at varying operating conditions due to complex modes [13]. The accurate information pertinent to the modes constituting complex oscillations leads to accurate determination of the impedance, therefore, enabling identification of the source of disturbance up/downstream of the interconnecting point. Therefore, it is of great interest to detect all possible modes using a systematic approach such that preventive measures can be employed and thus contribute to realistic self-healing and resilient power systems.

Assuming that the oscillations have a single mode (e.g. subSR), and are stationary in nature over a designed window,

it is relatively straightforward to detect its presence by using synchrophasors data, Discrete Fourier Transform (DFT) based algorithms [14], [15], and designing bandpass filters [16]. However, the constraints on reporting rate and superimposition of data with filters typically limit the observability of network disturbances constituted by modes with indistinct frequency bandwidths and inter-harmonic orders. An approach reported in [17], [18] proposed DFT based technique to detect the supSR modes while considering the theoretical constraints such as spectral aliasing and reporting rate limitation. This is only applicable if the event is stationary, modes are distinct and located within the defined bins of DFT spectra. Other methods employing waveform data for the nonlinear and non-stationary single mode SR-based oscillations are reported as Hilbert transform [19], Time Frequency (TF) transformation, and synchrosqueezing transformation (SST) [20]–[22]. However, the reported methods suffer from the non-reassigned pointing for the modes with strong frequency-proximity, thus the performance is further compromised with noise and strongly time-varying signals.

Amongst the different variants of power network oscillations, low-frequency oscillations have been extensively studied for modes detection and source localization [3]. Most of the methods consider the phasor measurement units (PMUs) data to measure the energy threshold over specified frequency bands [23], dissipating energy flow (DEF) t hrough t he node [24], and mode shape estimation approach [25]. The energy based method specifically r ely o n e xtensive b aseline studies to set the threshold for oscillation detection. However, such methods require two important considerations, i.e. a careful estimation of the threshold and accurate identification of frequency bandwidth. It is therefore explicitly challenging to determine a single universal threshold valid for the entire range of operating conditions. Similarly, the DEF method is an improved approach as compared to the original energy based approach as proposed in [26]. Similarly, its effectiveness has been demonstrated by testing simulated cases of sustained oscillations, including both poorly damped natural and forced oscillations and more than 30 actual events in ISO New England (ISO-NE) and two events in Western Electricity Coordination Council (WECC) systems. However, the variants of DEF also assume a single operating condition which is practically unrealistic as the operating conditions of IBRs-dominated networks significantly c hange a nd r esult in uncertain R/X ratios [27], [28].

In contrast, literature on the detection of SSCI-driven MSR oscillations and identifying the characteristics of their sources in a power network is limited. This is intrinsically justified by the limitation and fidelity o f a pproaches e stimating and reporting the modes using synchronized phasors and waveform data [29]. Similarly, computing the intact states of impedance for varying operating conditions becomes challenging when the modes involve frequency coupling. Extending the application of synchronized waveform measurement units (SWMUs) [30] to detect the MSR-based oscillations, this work offers a systematic method for identifying MSR oscillations using a novel realigned instantaneous frequency-based synchro transform (IFST) with adaptive window. The proposed method uses synchronized voltage and current waveforms typically available at the grid nodes and point of common coupling (PCC) of IBRs. Furthermore, this paper proposes a modes-based approach for the reconstruction of power flow at varying operating conditions to characterize and localize the participating sources of both active and reactive power oscillations in the network. The key contributions are summarized as follows:

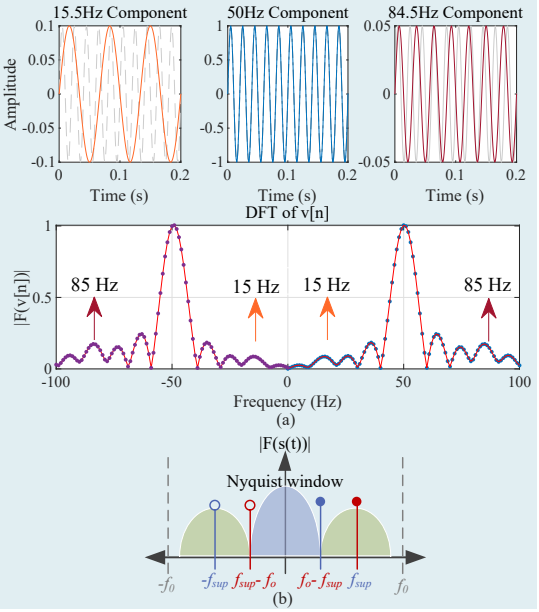

Fig. 2: Performance of DFT for undersampled signals (a) signal with 84.5 Hz and 15.5 Hz modes and its spectrum, (b) role of Nyquist window for $f_i > f_n/2$ modes, and the folded spectral magnitude.

- A novel realigned adaptive IFST (AIFST) is proposed to facilitate the accurate identification of complex oscillation modes at varying conditions of the power network.
- The admittance model subjugated by MSR due to coupled frequencies at the specific operating point conditions is derived from the reconstructed modes.
- Taking into account the reconstructed modes and the subsequent admittance model, the complex power flow is derived. This enables the characterization of the oscillation sources for the active/reactive oscillations in the network.

The remainder of the paper is organized as follows: Section II provides the motivation for this work, presenting the limitations of synchrophasors under multimode SR. Section III presents the proposed method; with results provided in Section IV. Section V concludes the paper.

II. Fidelity of PMU Based Observability

Electromagnetic oscillations originating due to control interactions of IBRs in weak grids have been a focus due to a limited understanding of their origin [3]. The presence of complex modes in SSCI based oscillation is different as compared to the mechanism of harmonics, low-frequency oscillations and forced oscillations due to time-varying frequency and damping characteristics. Typically, such oscillations involve a wide band of frequencies, where the dominating modes have coupled frequencies resulting in MSR-based oscillations [5]. They usually originate as a result of PLL response to

unbalanced grid conditions. Consequently, in such conditions the control system starts interacting with the power network components, resulting in complex oscillations, and making it challenging to detect.

This phenomenon is illustrated in Fig. 2 which is best aligned with Fig. 1 based on coupled frequency concept. The observability constraints of such disturbance in power networks using PMUs (instruments operating on DFT based approach) can be explained by assuming a non-stationary, multi-component signal with sub synchronous component of frequency f_{sub} and super synchronous component of frequency f_{sup}, originating as a result of SSCI. The instantaneous signal comprised of fundamental component (f_0) and accompanied by sub-synchronous and super-synchronous modes can be modeled as

$$x(t) = A_0 \cos(2\pi f_0 t + \phi_0) + \sum_{i=1}^{2} A_i e^{\sigma_i t} \cos(2\pi f_i t + \phi_i) \tag{1}$$

where A_0, f_0 and ϕ_0 denote the amplitude, frequency and phase of the fundamental component, the subsequent indexes ($i = 1, 2$) for A_i, f_i and ϕ_i corresponds to SSCI components (f_{sub}, f_{sup}), and σ_i represents the damping factor of each SSCI mode.

Typically, the reporting rate of PMUs for wide area monitoring systems (WAMS) is between $10-100\,fps$. Considering a PMU with a fixed sampling rate $f_R = 100 fps$, the expression in (1) at n^{th} sample can be expressed as

$$x(n) = A_0 \cos(2\pi \hat{f}_0 n + \phi_0) + \sum_{i=1}^{2} A_i e^{\hat{\sigma}_i n} \cos(2\pi \hat{f}_i n + \phi_i) \tag{2}$$

where $\hat{f}_0 = f_0/f_R$ and $\hat{f}_i = f_i/f_R$ is the normalized frequency of the fundamental and SSCI component, respectively. Similarly, $\hat{\sigma}_i$ denotes the damping factor normalized at the fixed sampling rate.

Conventionally, a rectangular window of length $N_R = f_R/f_0$ is applied to obtain synchrophasors using a DFT-based algorithm. The DFT window length and the sampling period determine the number of spectral bins and the respective inter-bin distance for the frequency components in (2). Therefore, considering $100\,fps$ reporting rate of PMU with fixed DFT window length, the fundamental and subsequent frequency components can be expressed in spectral bins as

$$\hat{f_n} = \frac{f_0}{f_R} = \sum_{i=0}^{2} \frac{\Upsilon_i}{f_R}, \tag{3}$$

where $\Upsilon_i = \Gamma_i + \hbar_i$ represent the spectral bin of frequency components and their inter-bin location for fundamental and subsequent SSCI based components depending on the index ($i = 1, 2\cdots$). Subsequently, $\pm\Upsilon_{sub}$ and $\pm\Upsilon_{sup}$ represent the spectral bins of SSCI components when synchrophasors with fundamental frequency (f_0 = 50/60 Hz) are generated using a rectangular window of length N_R for a signal presented in (2). The frequency component lie at integral bin for $\hbar = 0$ if $f_0 = \hat{f}_n$. However, for SSCI components where assuming $f_{sub} \in [1, 25]$ and $f_{sup} \in [60, 100]$, then $\Gamma_1 \neq \mathbb{Z} \,\&\, \leq 1$. Similar is the case for Υ_2, where $\Gamma_2 \neq \mathbb{Z}$ and this deduce $\hbar_i \neq 0$ which implies f_0 and subsequent f_i components do not lie on integral bins and estimated synchrophasors are affected with spectral leakage as illustrated in Fig.2.

The DFT spectrum of (1) for f_0 and superimposed by f_{SSCI} components is constituted by their respective positive and negative spectra [14], given as

$$[\nu] = \nu[k, \Gamma]^{\pm}_{f_0} + [k, \Gamma]^{\pm}_{f_{SSCI}} \tag{4}$$

(4) can be written for the $\pm\Gamma$ and using rectangular window taking sample at each n^{th} interval as

$$\check{\nu}[n, \Gamma]^{\pm}_{f_0} = \hat{A}_0 \cos\left(2\pi \frac{\Gamma_0}{f_0 \cdot N_R}(n + \Gamma_0) + \phi_0\right) e^{-j2\pi \frac{\Gamma_0}{f_0}} \tag{5}$$

$$\check{\nu}[n, \Gamma]^{\pm}_{f_{SSCI}} = \frac{1}{f_i \cdot N_R} e^{\frac{\hbar_i}{N_R}} \left[\sum_{i=1}^{f_i - 1} \hat{A}_i e^{\frac{\hbar_i}{N_R}} \cos\left(2\pi \frac{\Gamma_i}{f_i \cdot N_R}(n + \Gamma_i) + \phi_i\right) e^{-j2\pi \frac{\Gamma_i}{f_i}}\right] \tag{6}$$

(5) and (6) can be simplified using Euler identity to normalize the estimated phasors for corresponding reporting of synchrophasors algorithm, well derived in [10]. Therefore, this can be written as

$$\begin{aligned} \Psi_0(\Gamma_0 + n) &= \frac{1 - e^{j2\pi(\Gamma_0 + n)}}{1 - e^{j2\pi\left(\frac{\Gamma_0 - n}{f_0}\right)}}, \\ \Psi_i(\Gamma_i + n) &= \frac{1 - e^{j2\pi(\Gamma_i + n) + \frac{\hbar_i}{f_n}}}{1 - e^{j2\pi\left(\frac{\Gamma_i + n}{f_n}\right) \cdot \frac{\hbar_i}{f_n}}}, \end{aligned} \tag{7}$$

where Γ_0 and Γ_i denote the bin distance between f_o, f_{SSCI} in (1) and any n^{th} positive sequence harmonic content that illustrates the MSR and non-stationary complex signal. (7) implies that $\Psi_{(0,i)}$ for f_o and f_{SSCI} depends on the sampled signal reported at n^{th} interval by the synchrophasor. This leads to two important conclusions

- The synchrophasor-based estimation algorithm primarily depends on the f_o and assumes that $[\nu]$ has finite stationary cycles over the applied window.
- For any f_{SSCI} with $\omega_i(t) \neq \mathbb{Z}$ constituting $\nu[n]$ with $\sum_{i=1,2\cdots}^{t=0:k:1} \hat{A}_i cos(w_i t + \phi_i)$ as superimposed components, the N_R doesn't guarantee the minimum conditions for Nyquist theory.

This implies that if $N_R \ll 2f_{SSCI}$, the spectrum of frequencies for f_0 and f_{SSCI} folds up at each respective $\pm\Gamma$, and results in aliased spectral leakage as illustrated in Fig. 2(a, b). This affects the accurate estimation of synchrophasors which subsequently leads to erroneous estimation of the associated parameters, consequently misleading the impedance proportional to the respective modes and nominating the wrong candidate as a source of disturbance in the network.

III. Proposed Method

Time synchronised waveforms (also referred to as synchro-waveforms [30]) and AIFST are employed to determine the complex and non-stationary modes, followed by the identification of the sources to characterize their participation for either injecting or absorbing oscillations in an IBR-based

network. The method is described in detail in the following sub-sections.

A. Mathematical Background of SST

Assuming a non-stationary time-varying complex signal as illustrated in (1), we transform it into the time domain to facilitate the derivation and its Fourier Transform (FT), written as

$$X(\omega) = \int_{-\infty}^{+\infty} x(t) e^{-jwt} dt \tag{8}$$

The short-time Fourier transform (STFT) of $x(t) \in L^2(\mathbb{R})$ for real and even sliding window $g_\sigma \in L^2(\mathbb{R})$ is given as

$$S(t,\omega) = \int_{-\infty}^{+\infty} x(u) e^{-\jmath\omega(u-t)} g_\sigma(u-t) dx \tag{9}$$

STFT calculates the FT of $x(t)g_\sigma(u-t)$ for shorter duration as $u \in [t-\Delta^t, t+\Delta^t]$. Therefore; for STFT it is essential to assume that the magnitude and phase components of the signal in (1) fulfill the criteria of $|A_i'(t)| \leq \varepsilon$ and $|\phi_i''| \leq \varepsilon$, where ε is a sufficiently small value. In addition, the components of the signal $x(t)$ should have sufficient separation distance as $2\Delta_\omega < \phi_k'(t) - \phi_{k-1}'(t)$ satisfies only if $\phi_{0,i}' \in x(t)$ are weakly time varied. With this condition, (1) is considered as a weakly time-varied sinusoidal signal and is approximated to have only harmonic components for all duration of u [31]. Using Taylor expansion, (9) can be modified for (1) and can be approximated for a fixed time interval ($\hat{t}$) as

$$\begin{aligned} S(t,\omega) &= \int_{-\infty}^{+\infty} g_\sigma(u-\hat{t}) A(\hat{t})\, e^{\jmath\left(\phi(\hat{t})+\phi'(\hat{t})(u-\hat{t})\right)} e^{-\jmath\omega(u-\hat{t})} dx \\ &= A(\hat{t}) e^{\phi(\hat{t})} \hat{g}_\sigma(\omega - \phi^{'}(\hat{t})) \end{aligned} \tag{10}$$

(10) is generalized for fundamental (A_0, ϕ_0) and subsequent terms (A_i, ϕ_i) reflecting (9) and the components of $x(t)$. We further replace $\hat{t}$ with t for ease of simplicity, while detailed mathematical derivation can be seen from [31]. This leads to the estimation of IF ($\phi^{'}$) in time-frequency frame with (t,w) as

$$\begin{aligned} \breve{\omega}_x(t,w) &= \Re e \left\{ \frac{\delta_t\, S(t,w)}{\jmath\, S(t,w)} \right\} \\ &= \Re e \left\{ \frac{\delta_t\, A_0(t) e^{\jmath\phi_0(t)} \hat{g}_\sigma(\omega - \phi_0{}'(t))}{\jmath\, A_0(t) e^{\jmath\phi_0(t)} \hat{g}_\sigma(\omega - \phi_0{}'(t))} \right. \\ &\quad \left. + \frac{\delta_t\, A_i(t) e^{\jmath\phi_i(t)} \hat{g}_\sigma(\omega - \phi_i{}'(t))}{\jmath\, A_i(t) e^{\jmath\phi_i(t)} \hat{g}_\sigma(\omega - \phi_i{}'(t))} \right\} \\ &\quad \text{where by solving for } \delta_t, \\ &= \phi_0'(t) + \phi_i'(t), \end{aligned} \tag{11}$$

where $\Re e$ is the real part of $\breve{\omega}_v(t,w)$. (10) and (11) provides a biased estimate of the modes in $x(t)$, with the unsymmetrical alignment of $\phi(t)^{'}$ to $|A(t)|$ and the energy concentration scatters around the ridges. To gain concentrated information and squeeze energy in the region around the coefficients $\forall\, \phi_i \in x(t)$, the reassignment operator can be employed as Dirac delta function for ω as

$$\tilde{T}(t,\psi) = \int_{-\infty}^{+\infty} S(t,\omega)\delta\left[\psi - \breve{\omega}_x(t,w)\right] d\omega \tag{12}$$

Therefore, substituting (10) and (11) into (12) provided that condition for sufficient separation of modes is met, the coefficients are reallocated from $S(t,w) \rightarrow (t, \breve{\omega}_S(t,w))$ using the coefficient reconstruction as

$$\breve{a_k}(t) \approx \frac{1}{2\pi g_\sigma} \int_{|\omega - \phi_k'(t)| < \tau_{SSCI}} \tilde{T}(t,\psi) d\psi \tag{13}$$

This implies the following argument proved in [32]

$$\frac{1}{2\pi g_\sigma} \int_{|\omega - \phi'{}_k(t)| < \tau_{SSCI}} \tilde{T}(t,\psi) d\psi - \breve{a_k}(t) \leq \kappa\tilde{\varepsilon} \tag{14}$$

where τ_{SSCI} controls the bandwidth for reconstructing the coefficients, κ is a constant, and $\varepsilon << 1$ is a precision for ensuring that each component is reconstructed with a tiny error, and the coefficients are tightly concentrated in their respective bands $(t, \phi_k^{'}(t))$.

To extract a concentrated coefficient with intact information, the STFT is iterated to obtain SST, however, it has the following limitations:

- The input signal for SST is assumed to be weakly varying in time, an assumption impractical for IBR-dominated networks. As a result, any input signal with non-stationary oscillations is approximated as a counterpart of harmonic oscillations for determining the SST coefficients.
- SST employs a fixed window that is insufficient for acquiring concentrated information around ridges for calculating the coefficients. A small window size for high frequencies and a larger window size for for lower frequencies is a requirement to compute the exact modes.

B. Adaptive SST

The energy concentration of SST is improved by an iterative process of STFT using a constant window. The concentration around ridges still deteriorates when subject to strong noise and time-varying signals. In-depth mathematical analysis discussing the limitations of constant window-based SST operation and challenges associated with acquiring the higher resolution TFr of MSR-enforced multi-component signal is presented in [33]. Therefore, an adaptive time-varying window is considered for this study. We begin this by considering a Gaussian window whose Fourier transform is given as

$$\hat{g}_\sigma(t) = \frac{1}{\sqrt{2\pi}\sigma} e^{\frac{-t^2}{2\sigma^2}} \tag{15}$$

where, σ is computed as $\sqrt{\frac{\sum |t-\bar{t}|^2}{n-1}}$ at each $n-1$ sample of N. Based on (15), (10) can be rewritten as

$$S(t,\omega) = \int_0^{\infty} A(t+u) \frac{1}{\sqrt{2\pi}\sigma} e^{\frac{-u^2}{2\sigma^2}} e^{-j\omega u} du \tag{16}$$

To facilitate the derivation, a constant chirp signal-based approximation of $x(t)$ is considered as $x(t) = Ae^{\left[\phi_0(t)+\phi'(t)(u-t)+\frac{1}{2}\phi''(t)(u-t)^2\right]}$ [34] that yields

$$= \int_{-\infty}^{+\infty} Ae^{j\left[\phi_0(t)+\phi_0'(t)u+\frac{1}{2}\phi_0'(t)w^2\right]} \frac{1}{\sqrt{2\pi}\sigma} e^{-\frac{u^2}{2\sigma^2}} e^{-j\omega u} du \tag{17}$$

$$= \frac{A}{\sqrt{2\pi}\sigma} e^{j\phi_0(t)} \int_{-\infty}^{+\infty} e^{-\frac{1}{2}\left[\frac{1}{\sigma^2} - j\phi'_\emptyset(t)\right]u^2 - 1[\omega - \phi_\circ(t)]u} du \quad (18)$$

The partial derivative of 18 yields

$$\partial x(t,\omega) = x(t,\omega)\left\{ j\phi'(t) + \frac{\phi''(t)[\omega - \phi'(t)]}{\frac{1}{\sigma^2} - j\phi''(t)} \right\} \quad (19)$$

Substituting (19) in (11), the IF can be estimated as

$$\breve{\omega}_x(t,w) = \frac{\phi''(t)^2}{1+\phi''(t)^2}[\omega - \phi'(t)] + \phi'(t) \quad (20)$$

Implying the condition in (14), (20) can be written as

$$|\breve{\omega}_v(t,w) - \phi'(t)| < \varepsilon \left| 1 - \frac{1}{1+\phi''(t)^2} \right| \quad (21)$$

From (21), if the $x(t)$ has MSR components that are varying slowly in time, then ε is small enough to assume oscillation components as an approximation of harmonic order of $x(t)$. Therefore, the condition satisfies if $\breve{\omega}_v(t,w) = \phi'$, otherwise, it can be observed from (20), that the estimate of $\breve{\omega}_v(t,w)$ depends on $\phi''(t)$ which is rate of change of IF. It is clear that for slow variation, the $\phi''(t)$ is small and is negligible, however for strongly time-varying signals, the $\phi''(t)$ is large enough to provide a biased estimate of IF using (20). Therefore, the continuous iteration of (20) provides concentrated TFr with reduced error between $\breve{\omega}_v(t,w)^N$ and $\breve{\omega}_v(t,w)^{N-1}$ for optimal solution of $\tilde{\varepsilon}$. This is expressed as

$$\tilde{T}(t,\psi) = \int_{-\infty}^{+\infty} S(t,\omega)\delta\left[\psi - \breve{\omega}_v^N(t,w)\right] d\omega < \varepsilon \quad (22)$$

In theory, the above solution converges as the TF coefficients are reassigned to $(t,\breve{\omega^N})$, however, the frequency estimator in discrete implementation is rounded to the nearest $\mathbb{Z}$ to satisfy $\omega = \phi^{'}(t)$. This leads to a non-realignment issue with IF estimators $(\breve{\omega^N})$ and results in a deviated approximation of MSR modes in discrete implementation. Therefore, we ensure that the IF estimator is correctly aligned to its realignment region for approximation of all MSR (ϕ^i) modes. It is intrinsic to ensure accurate reference for obtaining the accurate estimation of ω. Therefore, we further modify the reassignment operator as $\delta[\omega - \breve{\omega}(\hat{t})]$ provided by [31]. This modification has the effect of sharpening the frequency localization of the SST and reducing the interference between adjacent frequency components, resulting in a clearer and more interpretable TFr of the signal. The new reference can be written as $\tilde{w}_{ref} = \breve{\omega}(\hat{t}) - \omega = 0$. It is best to center align the IF estimator across each MSR component present in $x(t)$, this allows the location of the band center of all MSR components before the realignment of $\breve{\omega}(\hat{t})$ [33]. Therefore, (11) is discretized at $k = (1,2,\cdots,K)$ and can be formulated for IF band center as

$$\tilde{w}_{ref} = \left\{ k_\omega \;\middle|\; \begin{array}{l} \Delta k_\omega > |\breve{\omega}_v(t,k_\omega) - k_\omega| \\ 1 > \partial_\omega \breve{\omega}_x(t,k_\omega) \\ |\breve{\omega}_v(t,k_\omega) - k_\omega + 1| \geq |\breve{\omega}_v(t,k_\omega) - k_\omega| \end{array} \right\} \quad (23)$$

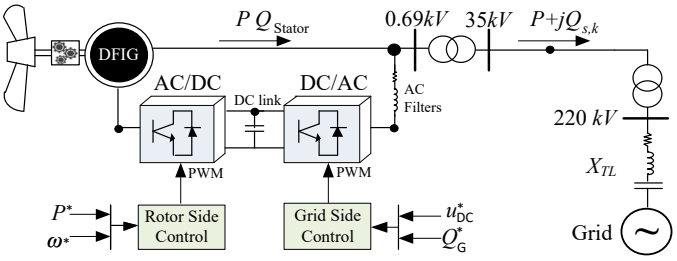

Fig. 3: A schematic of DFIG connected with the grid through a compensated transmission line (X_{TL}).

Here, $\tilde{w}_{ref} \subset \omega$ such that $\omega \in \left[\tilde{w}^{+}_{ref}, \tilde{w}^{-}_{ref}\right]$, and limits of $\Delta\tilde{w}_{ref} = \tilde{w}^{-}_{ref} < \omega < \tilde{w}^{+}_{ref}$. The boundary limits of the new IF for the k^{th}_{ω} bandwidth can be written in discrete domain as

$$\Delta\tilde{w}_{ref} = \left\{ \begin{array}{ll} \tilde{w}^{-}_{ref}, & \max\delta_\omega\breve{\omega}_v(t,k_\omega) \geq 1 || \ \omega < \tilde{w}^{i}_{ref} \\ \tilde{w}^{+}_{ref}, & \min\delta_\omega\breve{\omega}_v(t,k_\omega) \geq 1 || \ \omega > \tilde{w}^{i}_{ref} \end{array} \right. \quad (24)$$

where the subscript $i = [1,2\cdots]$ refers to frequency bands of the corresponding MSR modes. From (24), the IF estimator can be realigned across $i = [1,2\cdots]$ bands of frequencies in (8) and $\breve{\omega}_v(t,w)$ for i^{th} modes is written as

$$\breve{\omega}_v(t,w) = \left[\begin{array}{ll} \breve{\omega}_v(t,k_\omega)_{i=1}, & \tilde{w}^{-}_{ref,i=1} < k^{th}_{\omega} < \tilde{w}^{+}_{ref,i=1}; \\ \vdots & \vdots \\ \breve{\omega}_v(t,k_\omega)_{i=n}, & \tilde{w}^{-}_{ref,i=n} < k^{th}_{\omega} < \tilde{w}^{+}_{ref,i=n}; \end{array} \right. \quad (25)$$

where $\tilde{w}^{\pm}_{ref,i}$ refers to the frequency boundries of IF bands of $\breve{\omega}_v(t,w)$ aligned at its center. Therefore, the coefficients of STFT can be reallocated by using these realigned IF estimators across each frequency band's center as

$$\tilde{T}_v(t,\breve{\omega}) = \sum_{\frac{\Delta k_{\breve{\omega}}}{2} > |\breve{\omega}_v - k_{\breve{\omega}}|} S(t,\breve{\omega})\Delta k_{\breve{\omega}} \quad (26)$$

Following the realignment process for each mode, the coefficients in the discrete domain can be reconstructed as

$$\breve{a}_k = \frac{1}{2\pi g_\sigma(0)} \sum_{\tau_{SR} > |k_{\breve{\omega}} - \breve{\omega}|} \tilde{T}_v(t,\breve{\omega})\Delta k_{\breve{\omega}} \quad (27)$$

C. Sequence Reconstruction and Source Characterization

Assuming that all the branches and nodes connecting the IBRs and conventional power sources are well observable for a simplified network as shown in Fig. 3, the complex power for that specific node can be written as

$$S = \sum_{j=1}^{\ldots k} P_{j,k} + \Im \sum_{j=1}^{\ldots k} Q_{j,k} \quad (28)$$

where the terms k, j refer to the nodes in the network and operator "$\Im$" is the complex number. The active and reactive power at the nodes can be deduced from (28) as

$$\begin{aligned} P_{j,k} &= P_o + \sum_{i=1\cdots n} V_i I_i^* cos(\theta_{i,V} - \theta_{i,I}) \\ Q_{j,k} &= Q_o + \sum_{i=1\cdots n} V_i I_i^* sin(\theta_{i,V} - \theta_{i,I}) \end{aligned} \quad (29)$$

where P_o, Q_o refers to the fundamental frequency components, the subscript (i) refers to the modes (i.e., $subSR$,

$supSR$ and harmonic noise), and operator "$*$" refers to the conjugate. From (28) and (29), it can be said that the resultant power at any specific node is the sum of fundamental and non-fundamental components of the system. The identification of frequency modes relies on (26) and (27), however, characterizing the source for its active participation in SSCI oscillations is intrinsically dependent on the network admittance. The complex power for MSR-based oscillations is accurately observable if the system admittance is computed at that specific operating point. Previously, the source characterization for SSR and SSCI interaction is persuaded on the basis of a single operating point [27], [35]. However, it is not practical for an IBR-dominated network to consider a model solely derived for a single operating point [36]. This lacks confidence in deriving an accurate relation between the MSR and the system model. Therefore, the relation between the MSR modes and the admittance matrix (AM) obtained at varying operating points can be written as

$$\begin{bmatrix} v_{sub} \\ v_{sup} \end{bmatrix}_{(s,z_\kappa)} = \left[\boldsymbol{Y}_{(s,z_\kappa)}\right]^{-1} \begin{bmatrix} i_{sub} \\ i_{sup} \end{bmatrix}_{(s,z_\kappa)} \tag{30}$$

where i_{sub}, i_{sup}, v_{sub}, v_{sup} are sub synchronous and super synchronous current and voltage modes respectively, z_κ denotes the operating point condition and $[\boldsymbol{Y}]$ is the AM. The frequency coupled AM ($\boldsymbol{Y}_{FCAM}$) can be obtained by modifying (30) as

$$Y_{FCAM}(s,z_\kappa) = \begin{bmatrix} Y(s,z_\kappa)_{ii} & Y(s,z_\kappa)_{ij} \\ Y(s,z_\kappa)_{ji} & Y(s,z_\kappa)_{jj} \end{bmatrix} \tag{31}$$

where $\boldsymbol{Y}(s,z_\kappa)_{ii}$ and $\boldsymbol{Y}(s,z_\kappa)_{ij}$ represent the elements of the admittance matrix at the specific operating point (z_κ). For simplicity, (30) and (31) can be further manipulated by taking into account $[Y_{sub}](s,z_\kappa) = [i_{sub}] \times [v_{sub}]^{-1}$ and $[Y_{sup}](s,z_\kappa) = [i_{sup}] \times [v_{sup}]^{-1}$ at each operating condition (z_κ). The frequency coupled AM in (31) can be updated subsequently and in accordance with the obtained voltage and current modes. This can be written in a simpler form by representing in complex plane as

$$\begin{bmatrix} Y_{sub} \\ Y_{sup} \end{bmatrix}^i_{(s,z_\kappa)} = \begin{bmatrix} \boldsymbol{G}_{sub} + \Im \boldsymbol{B}_{sub} \\ \boldsymbol{G}_{sup} + \Im \boldsymbol{B}_{sup} \end{bmatrix}^i \tag{32}$$

Using (30), (31) and (32), the power for each MSR mode can be deduced as

$$\begin{bmatrix} s_{sub} \\ s_{sup} \end{bmatrix}^i_{(s,z_\kappa)} = \begin{bmatrix} \frac{i_{sub}^2}{Y_{ii}} + \frac{\Im\,(i_{sub}^* i_{sup}^*)}{Y_{ij}} \\ \frac{i_{sup}^2}{Y_{jj}} + \frac{\Im\,(i_{sub}^* i_{sup}^*)}{Y_{ji}} \end{bmatrix}^i \tag{33}$$

The $\boldsymbol{Y}_{ii}$ and $\boldsymbol{Y}_{jj}$, refers to WTG and grid side impedance, while the diagonal terms $\left(\boldsymbol{Y}_{ij} = \boldsymbol{Y}_{ji}^*\right)$ refer to the impedance due to coupled frequencies, respectively. Simplifying (33) further yields

$$\begin{bmatrix} s_{sub} \\ s_{sup} \end{bmatrix}^i_{(s,z_\kappa)} = \begin{bmatrix} i_{sub}^2 \\ i_{sup}^2 \end{bmatrix} \begin{bmatrix} 1/\boldsymbol{G}_{sub} + \Im \boldsymbol{B}_{sub} & 0 \\ 0 & 1/\boldsymbol{G}_{sup} + \Im \boldsymbol{B}_{sup} \end{bmatrix} \tag{34}$$

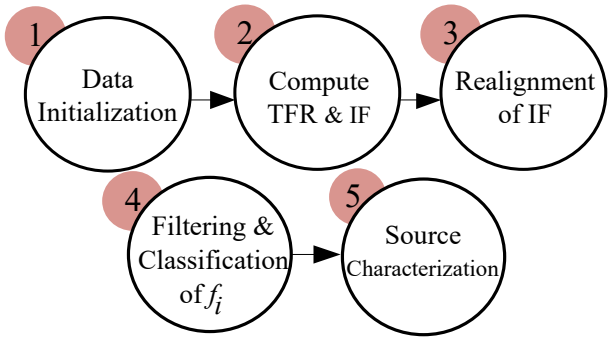

Fig. 4: Flow-chart of the proposed method

Subsequently, (28) can be modified using (34) to compute the MSR-based power either consumed or absorbed at the respective node as

$$\begin{aligned} S(s,z_\kappa) &= s_{sub} + s_{sup} = \boldsymbol{P} \pm \Im \boldsymbol{Q} \\ &= \left(\frac{i_{sub}^2}{\boldsymbol{G}_{sub}} + \frac{i_{sup}^2}{\boldsymbol{G}_{sup}}\right) \pm \Im \left(\frac{i_{sup}^2}{\boldsymbol{B}_{sub}} + \frac{i_{sup}^2}{\boldsymbol{B}_{sup}}\right) \end{aligned} \tag{35}$$

From (35), any IBR-induced oscillations in a weak grid can be a resultant of disseminating power at SSCI modes i.e., active and reactive power oscillation. The participating unit can inject or absorb either mode of the oscillations by varying the impedance of the node at that specific operating condition. Therefore, (35) concludes that negative $\boldsymbol{P}$ and $\boldsymbol{Q}$ implies the node as an active source of oscillations and vice versa.

To summarize, the overview of the proposed method is illustrated in Fig. 4, where the source and network can be characterized for SSCI power flow using five main steps as provided in algorithm 1. In the first step, the initialization is ensured to confirm the data meets the minimum sampling requirements and is well synchronized. This is achieved with SWMUs as they are capable of capturing data with high samples at nodes where the WTGs are connected. Therefore, we ensure that data at the central location is synchronized and has no missing data and outliers. If so, the bad and missing data is replaced with interpolation. In the second step, the SST is applied using (22). In this step, the preliminary information on instantaneous frequency ($\tilde{\omega}_v$) and phase ($\phi^{'}$) is obtained. In the third step, the $\tilde{T}(t,\psi)$ is obtained using (26) to retrieve the complex TFr. This is achieved by computing $\tilde{w}_{ref} = \tilde{\omega}(\hat{t}) - \omega = 0$ using (23). In this step $\tilde{\omega}_v$ is realigned to its centre location for each mode. This avoids mixing low and high-frequency modes and provides the complex TFr of the event. In the fourth step, the frequency modes are selected based on conditional selection and the SSCI modes are reconstructed using (27). Finally, the complex SSCI power flow is derived using (35) at that specific operating point. The characterization of the source is assessed by the direction of power flow derived from the SSCI modes. The efficacy of the proposed method is demonstrated through numerical examples and a detailed case study.

IV. Case Study

The proposed method is first verified using a synthetic signal to prove the detection accuracy in the presence of noise and time-varying frequencies, then its effectiveness is evaluated for real-world cases that exhibit SSR-driven oscillations and SSCI events. Dataset for two real events [37], one obtained through replication of an event through a PSCAD simulation and another recorded through PMUs, is used to verify the accuracy of modes detection. The detection accuracy is compared against methods recently reported in the literature, i.e., improved DFT (IpDFT) [17] and Prony analysis provided in [38]. Further, a modified IEEE-9 bus network is used to characterize the SSCI based power flow, replicating the ERCOT incident [39].

The identification and characterization algorithm is implemented in MATLAB/Simulink running on a desktop computer with a Core i7-11700 processor and 32GB random access memory. The algorithm takes an average computational time of 400 ms for the proposed method when the voltage and current waveforms are sampled at 1.6kHz. This sampling rate is sufficient enough to satisfy the Nyquist criteria for observing the complex SSCI modes up to 1kHz. The computational time increases to approximately 800 ms when the waveforms are severely contaminated by noise and harmonics.

Algorithm 1 Complex SSCI Detection & Characterization

STEP 1: `INITIALIZATION`
`Compute: ` $\hat{g}_\sigma$, `Length (N): of signal From` (1), `Sampling frequency (1/T), Nominal` f_0.
STEP 2: `COMPUTE STFT &` $\breve{\omega}_v$ ▷ using (22) & (21)
STEP 3: `REALIGNMENT OF IF`
for $t = 1 : N$ **do**
  Calculate $\tilde{w}_{ref}$ From (23)
  ▷ Compute k
  for $n = 1 : k$ **do**
    Compute $\tilde{w}^{+}_{ref}$ & $\tilde{w}^{-}_{ref}$ From (24)
    Calculate $\breve{\omega}_v$ From (25)
  end for
end for
Output: $\tilde{T}_v(t, \breve{\omega})$
STEP 4: `CLASSIFICATION OF` f_i
$f_i \leftarrow \breve{\omega}$ From (22)
while $f_i \in [f_{sub},\ f_{sup}] \times \mathrm{N}$ **do**
  if $f_i = [\tilde{T}_v(t, \breve{\omega})]^{\mathbf{2\times 1}}$ & **sum** $= 2 \cdot f_0$ **then**
    $[X]^{\mathbf{2\times 1}} \leftarrow \breve{a}_k$ ▷ Multimode SSCI
  else if $f_0 \leq f_i$ & $f_i \notin [n^{th} \cdot f_0]$ **then**
    $f_{sup} \leftarrow f_i$
    $X \leftarrow \breve{a}_k$ From (27)
  else if $f_i \leq f_0$ & $f_i \notin [n^{th} \cdot f_0]$ **then**
    $f_{sub} \leftarrow f_i$
    $X \leftarrow \breve{a}_k$ From (27)
  end if
end while
STEP 5: `Source Characterization`
for $t = 1 : N$ **do**
  $X \in \mathbb{R}$
  while $|X| \neq 0$ **do**
    Compute Admittance Matrix From (32)
    Compute Power Flow From (35)
  end while
end for
for $i = 1 : j$ **do**
  $S(s, z_\kappa)^i$ Find power flow direction
end for

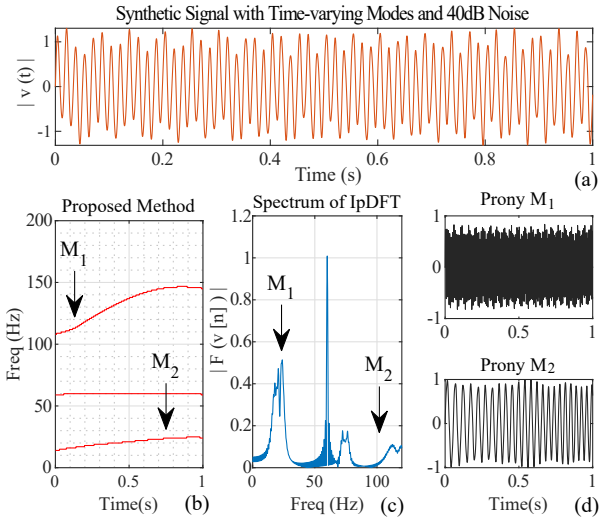

Fig. 5: Modes detection in strongly time varied sinusoidal signal as shown in (a), using (b) TFr of the proposed method, (c) Spectrum of IpDFT, (d) Prony method.

A. Verification through Synthetic Data - *Case I*

We first verify the accuracy of the proposed method for a synthetic signal having time-varying frequency modes as M_1 and M_2, where M_1 varies from 13.80 Hz→23.89 Hz and M_2 as 104.93 Hz→145.75 Hz with time. The signal is further corrupted with 40 dB noise and interharmonic components of magnitudes less than 1% to achieve an overall THD of 7.3%. Fig. 5 shows the modes detection comparison using the proposed method (AIFST), IpDFT, and Prony method. The TFr of the synthetic signal is obtained using the proposed method and shown in Fig. 5b. It can be observed that AIFST detects the modes with high accuracy as compared to IpDFT and Prony methods as shown in Fig. 5c and Fig. 5d, respectively. Comparatively, the IpDFT performance significantly deteriorates when the input signal is constituted with time-varying modes and is affected by noise above 40 dB. It is clear from Fig. 5b, that the coefficients of DFT do not lie within the integral bins and so the exact magnitudes at corresponding frequencies cannot be determined. In contrast, the Prony method requires a large window to estimate the modes in the signal. In addition to that, the modes M_1 and M_2 in this case are determined as an average over the period of the window and fail to provide accurate information on computing the frequencies at each operating interval. This limits the viability of the Prony method for constructing an admittance matrix for complex modes and at varying operating conditions. However, the proposed method precisely detects the modes (M_1, M_2) constituting the synthetic signals.

TABLE I: TABLE I: Identified Modes in Case I , Case II, Case III, Case IV, and Comparisons with IpDFT and Prony Method

Results	Case I: Simulation results of time varying modes with noise			Case II: Simulation results of the Hammi network without noise			**Case III**: Actual data of the Hammi network with noise only			**Case IV**: EMT simulation of ERCOT with harmonics and noise		
Methods	IpDFT	Prony	AIFST (Improved)	IpDFT	Prony	AIFST (Improved)	IpDFT	Prony	AIFST (Improved)	IpDFT	Prony	AIFST (Improved)
f_o	60	59.891	60	50	49.99	50	49.9935	49.9946	50	59.1022	59.6	60
f_{sub}	/	11.21, 27.55	13.8, 23.89	24.5753	24.5751	24.6008	8.287	8.2788	8.2570	12.11	11.3058	10.19
f_{sup}	/	100.83, 140.27	104.93, 145.75	75.4247	75.4252	75.4005	91.7129	91.6999	92.805	107.5998	108.7982	109.8

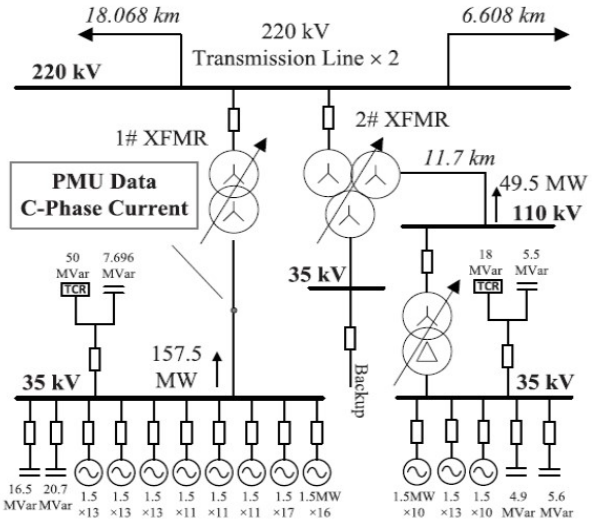

Fig. 6: Network of North China power grid experiencing SSO incident [37].

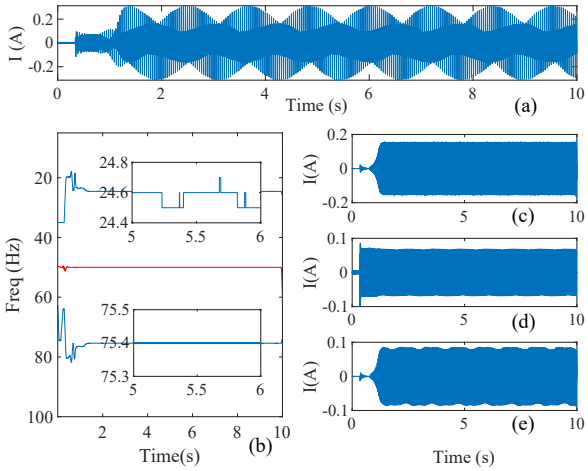

Fig. 7: Simulation result of Hami network showing, (a) instantaneous signal of current, (b) TFr of detected modes, (c) Mode at 24.6 Hz, (d) Mode at 50 Hz, (e) Mode at 75.4 Hz.

*B. Verification through Real World Dataset - **Cases II & III***

The accuracy of mode detection and its feasibility for real-world systems is further evaluated by selecting the Hami power grid in northwest China as shown in Fig. 6. The network comprises static VAR generators (SVGs), three wind farms based on type-3 WTGs, turbo generators and passive network components. The network has experienced two distinct SSCI events. For the first case, the instantaneous waveforms are obtained through PSCAD/EMTDC while incorporating factors producing the nearest replica of the event. Whereas, the dataset of the second event is recorded by both PMUs and waveform recorders [18], [37]. For both cases, the comparative evaluation of the proposed method with IpDFT and Prony analysis is presented next.

Case II: Fig. 7 (a) shows the current waveforms obtained through PSCAD/EMTDC simulation of the network shown in Fig. 6. Fig. 7 (b) shows the TFr of the SSCI event that occurs due to dynamic interaction between different network components, such as wind farms and SGs. The nearest estimation of f_o, f_{sub}, and f_{sup} using Prony analysis are 49.9 Hz, 24.575 Hz and 75.425 Hz, respectively. The TFr of Fig. 7 (a) shows a distinct mode having coupled frequencies (f_{sub} and f_{sup}) at 24.600 Hz and 75.400 Hz. The reconstructed modes at these frequencies are shown in Fig. 7 (c)-(e), and the key distinctions against both methods are summarised in Table (I).

Case III: The efficacy and sensitivity of the proposed method are further evaluated on the real data of the SSCI event as shown Fig. 8. A brief comparison is provided in Table (I) for the proposed, IpDFT and Prony method. It can be

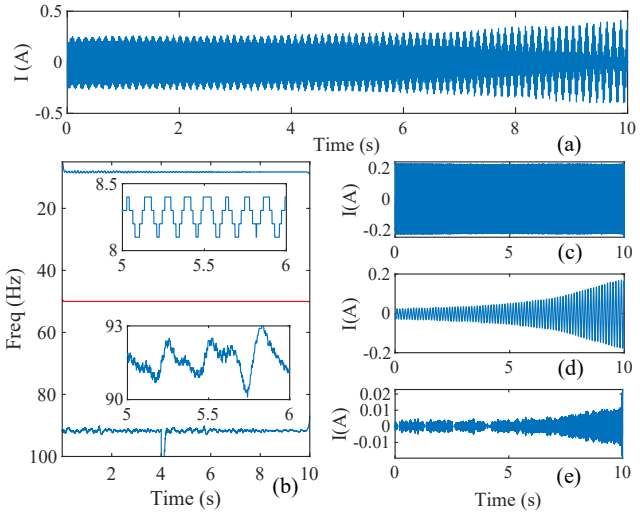

Fig. 8: Real data of SSCI event in North China grid showing, (a) instantaneous signal of current, (b) TFr of detected modes, (c) time-varying Mode at 8.4 Hz, (d) constant Mode at 50 Hz, (e) strongly time-varying Mode at 91.6 Hz.

concluded from the results that the ipDFT method reports the f_{sub} and f_{sup} only when the intact information on respective bins is constant and doesn't interpolate in the subsequent bins. Conversely, the Prony method estimates the nearest instantaneous frequency of both modes as $f_{sub} \rightarrow 8.278$Hz, $f_{sup} \rightarrow 91.6999$Hz, however, the mode detection subsequently deteriorate when strong variations in frequency are observed. Conversely, the proposed method is adaptive to frequency variations, flexibly adjusts the window and detects

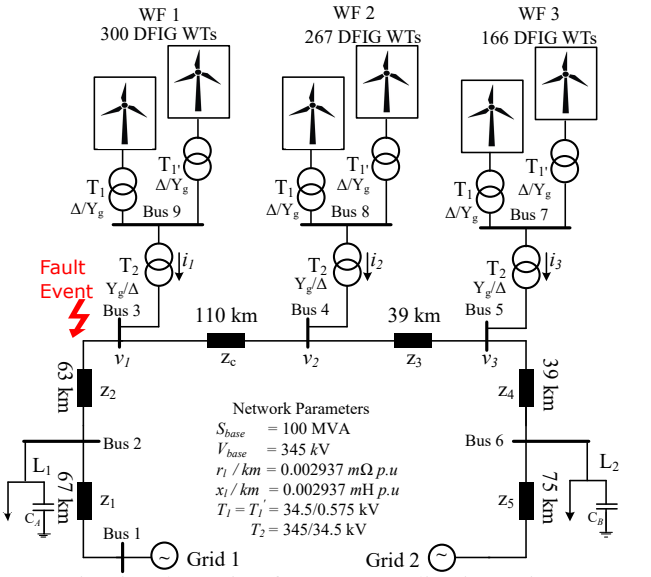

Fig. 9: Circuit schematic of ERCOT replication using IEEE 9 bus network.

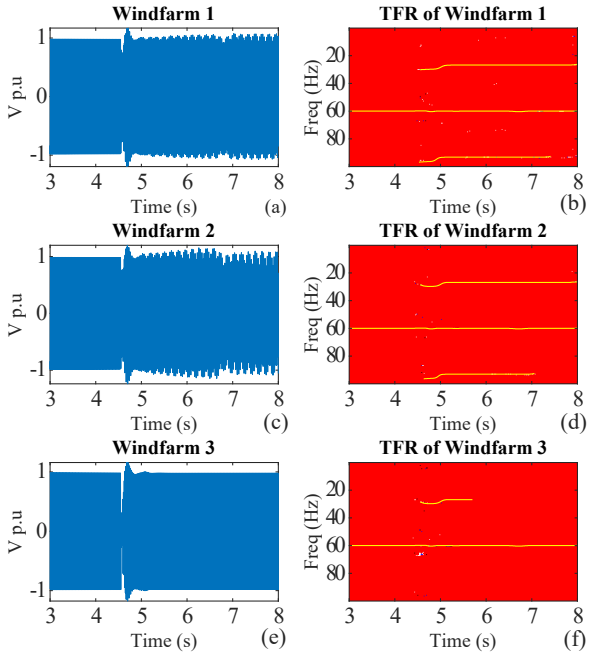

Fig. 10: Fault triggered SSCI showing voltage waveforms and TFr of modes obtained using AIFST for (a) WF1, (b) WF2, (c) WF3.

$f_{sub} \rightarrow 7.195$ Hz, $f_{sup} \rightarrow 92.807$ Hz, and consequently constructs the corresponding modes as shown in Fig. 8 (c-e). This concludes that both ipDFT and Prony methods capture the nearest modes if the noise ratio is above 40 dB. Furthermore, both approaches yield the mean values of the overlapping bins due to resolution limitations which inherently pose challenges in precise characterization of the modes. Alternatively, this can lead to indeterminacy of characterizing the SSCI source and deteriorate the overall identification and mitigation process.

C. Verification through Simulation Modelling - ***Case IV***

The testbed, as shown in Fig. 9, is based on an IEEE-9 bus system, developed by the University of Florida [39], incorporating real-time data to replicate the ERCOT network and reproduces the sub-synchronous oscillation event. The testbed has three wind farms of type-III configuration interconnected to 345kV substations. The transmission line specification and impedance data are obtained from [40]. We first validate the developed ERCOT model for the disturbance that produced the oscillation event. The event is initiated by a 3-phase fault leading to a line outage between Bus2 and Bus3. This outage leads to a radial connection between the series compensated line and wind farms connected at Bus3 and Bus4 as illustrated

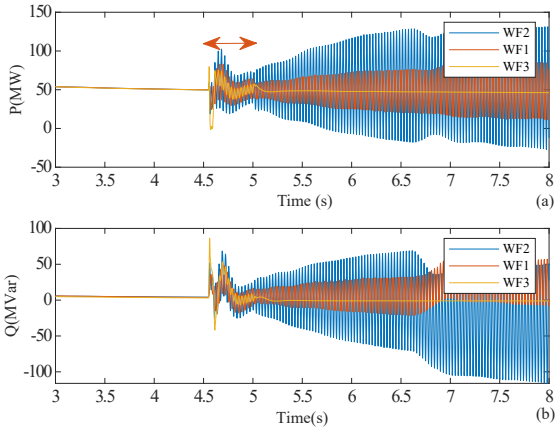

Fig. 11: Performance of Wind farms in response to fault triggering SSCI showing, (a) active power oscillations, (b) reactive power oscillations.

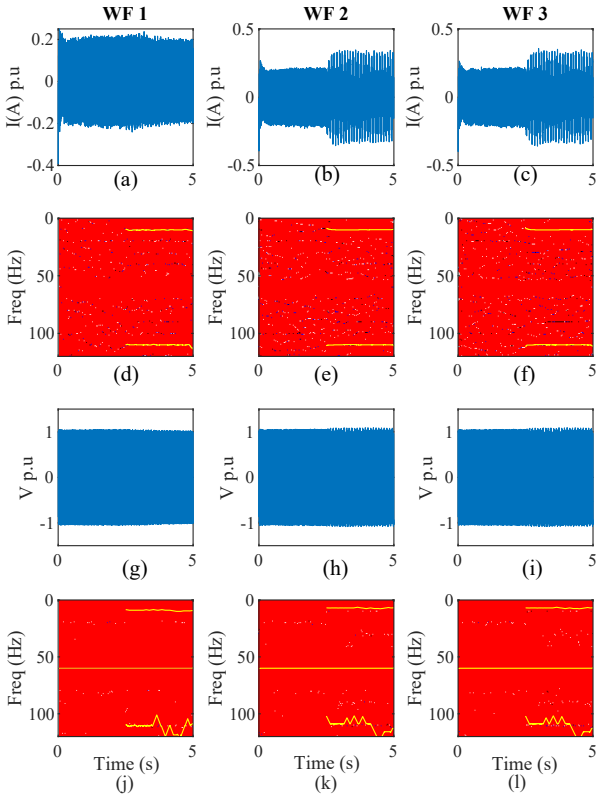

Fig. 12: Wind triggered SSCI showing, (a-c) current waveforms, (d-f) TFrs of detected modes in current waveforms, (g-i) voltage waveforms, (j-l) TFrs of detected modes in voltage waveforms.

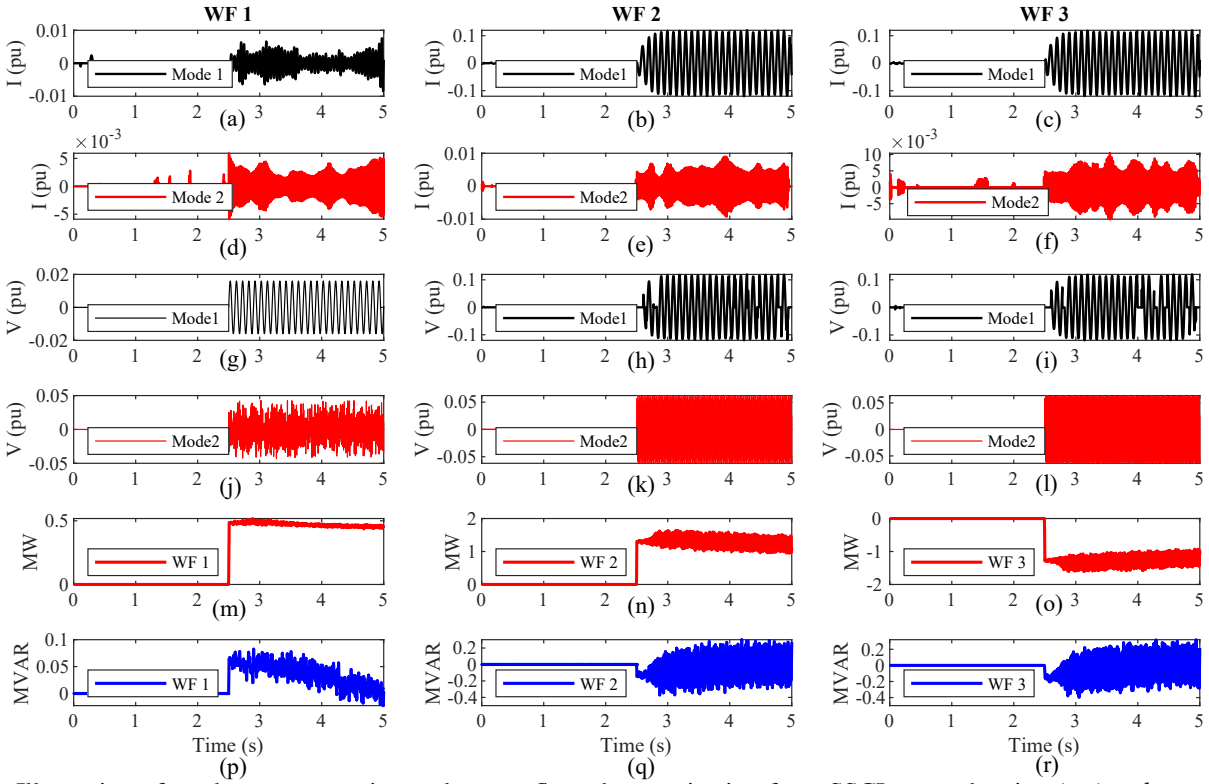

Fig. 13: Illustration of modes reconstruction and power flow characterization from SSCI-event showing:(a-c) sub_{SR} modes in current for WFI, WF2 and WF3, (d-f) sup_{SR} modes in current for WFI, WF2 and WF3, (g-i) sub_{SR} modes in voltage for WFI, WF2 and WF3, (j-l) sup_{SR} modes in voltage for WFI, WF2 and WF3, (m-o) active power flow at detected modes for WFI, WF2 and WF3, (p-r) reactive power flow at detected modes for WFI, WF2 and WF3.

in Fig.9. The voltage profiles obtained through simulation results on buses connecting the WTGs are shown in Fig.10. The instantaneous values are sampled at 1.2 kHz and the TFrs obtained through AIFST are shown in Fig.10(b d f). These results demonstrate and provide the early intervention of SSR modes at those particular nodes due to network disturbance. It is evident from Fig.10, that fault perturbs the voltage on all nodes, however, the oscillations emerge due to alteration in the topology of the network. In addition to that, the authors in [27], [39] analyze this event with a DFT-based algorithm which consequently estimates only subSR modes due to its bandwidth limitations. However, analyzing such an event using the proposed method demonstrates an additional mode involved in the SSCI-based oscillations as shown in Fig.10(b, d, f). The TFRs show that fault initiates control interaction and affects all three WFs as depicted in Fig.11. The WF3 mitigates the effect by damping these oscillations prevailing stable active/reactive power. However, it becomes prevalent that the isolation of the faulty section leaves WF1 and WF2 in radial connection with the line compensation (Z_c) as depicted in Fig.9. The triggered SSCI modes show that WF1 and WF2 have the highest contribution of subSR and supSR modes. On the other hand, the TFR of WF3 shows only subSR mode lasting for $500\,ms$ approximately. Therefore, this approach is an early contribution to suggest that the limitation and measurement fidelity of the DFT-based approach provide only a single subSR mode. Conversely, the accurate estimation and modes detection approach with the capability being adaptive to variance in frequencies for different operating conditions suggest coupled-frequency-based modes for the event. It is clear from the topology of the network that WF1 and WF2 are in radial connection of the series compensation and provide sufficient evidence of being involved in SSCI-driven oscillations.

On the contrary, this becomes severely challenging if the network components are not isolated, oscillating and threatening the whole network with explicit variations in the active/reactive power regulation. Therefore, to verify the proposed method for deriving SSCI based power flow due to IBRs injecting both $subSR$ and $supSR$ modes in a network, we further modify the network by tunning the parameters as listed in Table II.

The key results from this test can be concluded as follows: Fig. 12 illustrates the current and voltage waveforms of windfarms connected at Bus 9, 8, 7 for the network shown in Fig. 9. The instantaneous values are sampled at 1.2 kHz at their respective nodes for modes identification and SSCI source characterization. The TFrs of the current and voltage waveforms are shown in Fig 12 (d-f) and Fig. 12 (j - l), respectively. The system parameters and control variables are deliberately tuned to induce harmonics and noise in the current and voltage waveforms to verify the sensitivity and efficacy of the proposed method against noise discrimination. At $t = 2.5$ s, the SSCI oscillations start in the system by varying the wind speed from 11 m/s to 7 m/s. Fig. 13 (a, d), Fig. 13 (b, e) and Fig. 13 (c, f) present the corresponding MSR modes for current values, while Fig. 13 (j, m), Fig. 13 (k, n) and Fig. 13 (l, o) present modes for voltages obtained at interconnecting nodes of WF1, WF2 and WF3, respectively.

TABLE II: Wind Turbine Parameters for Test-Case III

Parameter	Value (SI)	Per-unit (pu)
Rated power	1.5MW	0.9
DC-link voltage	1150 V	
Rated voltage	575 V	1
Nominal freq.	60 Hz	1
Wind speed at Pmax	11 m/s	
$L_{ls}\,(X_{ls})\,, R_s$	94.5μH, 5.6 mΩ	$0.18, 0.023$
$L'_{lr}\,(X'_{lr})\,, R'_r$	84.0μH, 3.9 mΩ	$0.16, 0.016$
$L_m\,(X_m)$	1.5mH	2.9
Inertia, poles	$8.03H, 6$	
Friction factor	0.01	
C_{dc}	10mF	$0.3, 0.03$
$L_c\,(X_{Lc})\,, R_c$	0.16mH, 0.59 mΩ	0.267
$C_1\,(B_1)$	2.9mF	$K_{pig} = 0.83, K_{iig} = 5$
Current control (GSC)		$K_{pdc} = 8, K_{idc} = 400$
DC-link control		$K_{pac} = 8, K_{iac} = 400$
V_{ac} control		$K_{pir} = 0.6, K_{iir} = 8$
Current control (RSC)		$K_{pq} = 0.4, K_{iq} = 40$
Q control		$K_{p\text{PLL}} = 60$
PLL		$K_{i\text{PLL}} = 1400$

The characterization of SSCI source is persuaded on the basis of the power flow direction. From (35), the power flow is solely derived based on detected SSCI modes for the network shown in Fig.9. Further, the admittance matrix in alignment with the coupled frequencies is constructed from these modes, and the corresponding complex admittance is computed. According to the definition of (35), the substantial indications regarding the SSCI power flow determine the participant of highest contribution of particular SSCI power, so the source characterization can be concluded from Fig. 13 (m, p), Fig. 13 (n, q) and Fig. 13 (o, r), analysing the active and reactive power flow at each interconnected node of respective windfarms. It is important to recall from (35) that the absolute positive value of $S(s, z_k)$ for any network component determines it as the sink of the SSCI power (active/reactive) at that node, and vice versa. From Fig. 13 (o, r), the reconstructed SSCI modes show that WF3 has active and reactive power oscillations in the network with a major contribution of -1.4 MW active power and -0.15 MVAR reactive power. The negative sign illustrates that WF3 has injected both active and reactive power oscillations into the network at SSCI modes. The ranking of WF3 as a source of both active and reactive power oscillations is decided by the cumulative value of $S(s, z_k)$ in (35). Conversely, the active powers reconstructed from the SSCI modes for WF1 and WF2 are positive and are illustrated in Fig. 13 (m, n). Thus, according to (35) and source-sink criteria, the positive active power oscillations of 0.45 MW for WF1 and 1.2 MW for WF2 rank them as the sink of active power oscillations in the network. Similarly, the SSCI based reactive power for WF1 and WF2 is illustrated in Fig.13 (p ,q), respectively. Interestingly, it can be observed that WF1 acts as a sink of reactive power oscillations initially, and gradually starts to inject reactive power oscillations into the network. This behavior is in alignment with the induction generator effect, where the rotor side resistance of the generator gradually mimics large negative resistance as a consequence of the unstable dq control loop. Therefore, from (35) and SSCI based active-reactive power flows as illustrated in Fig.13, the $S(s, z_k)$ for WF1 is "$\boldsymbol{P} \pm \Im \boldsymbol{Q}$"; WF2 is "$\boldsymbol{P} - \Im \boldsymbol{Q}$"; and WF3 is "$-\boldsymbol{P} - \Im \boldsymbol{Q}$". Thus, $S(s, z_k) < 0$ for WF3 means that it is the source of both active and reactive power oscillations at SSCI. Similarly, the "$\boldsymbol{P} - \Im \boldsymbol{Q}$" for WF2 and WF1 suggest that they are participating in the network at SSCI as the sink of active power oscillations and source of reactive power oscillations. Therefore, it can be concluded from the power flows that all three WFs behave either as a source or sink of active/reactive power or both and vice versa at SSCI frequency.

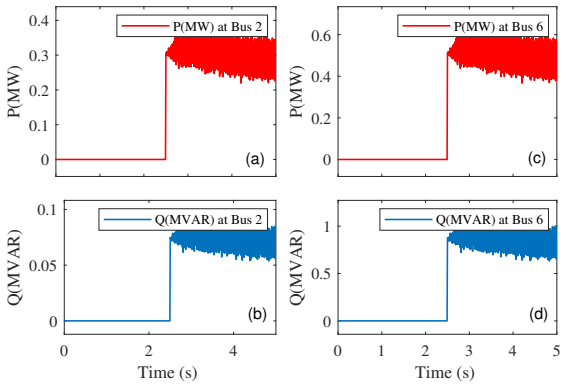

Fig. 14: SSCI based power flow: (a-b) active and reactive power on Bus 2; (c-d) active and reactive power on Bus 6.

It is important to highlight that the reconstruction of SSCI based active/reactive power flow for each source in the network explicitly directs toward the involvement of control loops in the IBRs. Therefore, the quantified and substantial power flow at SSCI modes for each WFs indicates hints toward inherent iteration in the control loops of the IBRs. Furthermore, the SSCI-based power flow for bus 2 and bus 6 of the network shown in Fig. 9 is illustrated in Fig. 14. It can be observed that $S(s, z_k) > 0$ for both buses (i.e. bus 2 and bus 6), indicating that these parts of the network actively absorb the SSCI oscillations. Consequently, it can be concluded that SSCI oscillations arise from wind farms and disperse active/reactive power throughout the entire network. The grid units, including synchronous generators and loads connected at the far ends of the network, thus act as absolute sinks for these oscillations.

Further, the comparative evaluation of the proposed method in contrast to IpDFT and Prony demonstrates that both techniques determine all the modes (f_o, f_{sub}, f_{sup}). However, this accuracy is contingent upon the condition that the data under the applied window is not time-varying and the noise ratio is considerably low as shown in Fig. 7. Otherwise, this results in an inadequate estimate of the f_{sub}, f_{sup} and its associated parameters. This is demonstrated in Case III where control parameters are deliberately tuned to get 9.8%ThD. A 20 dB noise in the voltage and current waveforms is further included to examine the sensitivity for real-world complex systems. It is evident from the comparative data in Table. I, that the proposed method provides an accurate estimate of all frequencies and associated parameters, such as phase and impedance, and consequently realizes appropriate characterization of the SSCI source.

V. Conclusions

This article proposes a systematic approach for deriving complex power flow and identifying sources associated with

SSCI-driven oscillations. First, it is analytically found that the detection of these oscillations using synchrophasors and DFT-based algorithms leads to erroneous estimation of modes having time-varying frequencies. Then, the limitation of SST is highlighted using an analytical approach to ascertain that its performance is affected by noise and strongly time-varying signals. Consequently, AIFST is proposed to improve the accuracy of modes detection and the corresponding particulars of SSCI-driven oscillations can be estimated adaptively in the presence of noise. Based on the identified m odes at that particular operating point, a global admittance matrix is derived to identify the origin of SSCI-based oscillations. To identify the active/reactive source or sink of SSCI oscillations, modes-based power flow i s d erived a t e ach o bservable node and characterization is carried out based on the active/reactive power flow. T he p erformance o f t he p roposed a pproach is compared in four cases against the state-of-the-art methods by employing numerical simulations. The adaptivity and applicability for real-world applications are further demonstrated by using real-world data obtained from networks experiencing SSCI-driven oscillations. As a result, a new diagnostic tool to support IBR-dominated grids may be realized, supporting effective mitigation of SSCI-driven oscillations.

REFERENCES

[1] Offshore wind energy: a vital and viable new frontier for renewables. [Online]. Available: https://www.wsp.com/en-au/news/2022/offshore-wind-energy-viable-renewable-energy

[2] "Guidelines for Subsynchronous Oscillation Studies in Power Electronics Dominated Power Systems," CIGRE, Tech. Rep., 06 2023.

[3] J. Shair, X. Xie, L. Wang, W. Liu, J. He, and H. Liu, "Overview of emerging subsynchronous oscillations in practical wind power systems," *Renewable and Sustainable Energy Reviews*, 2019.

[4] L. Meegahapola *et al.*, "Review on oscillatory stability in power grids with renewable energy sources: Monitoring, analysis, and control using synchrophasor technology," *IEEE Trans. Ind. Electron.*, vol. 68, pp. 519–531, 2021.

[5] W. Ren and E. Larsen, "A refined frequency scan approach to subsynchronous control interaction (SSCI) study of wind farms," *IEEE Trans. Power Syst.*, vol. 31, no. 5, pp. 3904–3912, 2016.

[6] D. Shu *et al.*, "Sub-and super-synchronous interactions between statcoms and weak AC/DC transmissions with series compensations," *IEEE Trans. Power Electron*, vol. 33, pp. 7424–7437, 2018.

[7] H. Liu *et al.*, "Subsynchronous interaction between direct-drive PMSG based wind farms and weak AC networks," *IEEE Trans. Power Syst.*, vol. 32, no. 6, pp. 4708–4720, 2017.

[8] J. Adams *et al.*, "ERCOT experience screening for sub-synchronous control interaction in the vicinity of series capacitor banks," *2012 IEEE Power and Energy Society General Meeting*, pp. 1–5, 2012.

[9] L. Wang *et al.*, "Investigation of SSR in practical DFIG-based wind farms connected to a series-compensated power system," *IEEE Trans. Power Syst.*, vol. 30, no. 5, pp. 2772–2779, 2015.

[10] T. Zaman *et al.*, "Multimode synchronous resonance detection in converters dominated power system using synchro-waveforms." in *27th International Conference on Electricity Distribution (CIRED 2023)*, 2023, pp. 3620–3624.

[11] W. Liu, Z. Lu, X. Wang, and X. Xie, "Frequency-coupled admittance modelling of grid-connected voltage source converters for the stability evaluation of subsynchronous interaction," *IET Renewable Power Generation*, vol. 13, no. 2, pp. 285–295, 2019.

[12] L. Fan, "Inter-IBR oscillation modes," *IEEE Trans. Power Syst.*, vol. 37, no. 1, pp. 824–827, 2022.

[13] Kunjumuhammed *et al.*, "Electrical oscillations in wind farm systems: Analysis and insight based on detailed modeling," *IEEE Trans. Sustainable Energy*, vol. 7, no. 1, pp. 51–62, 2016.

[14] X. Yang *et al.*, "Interpolated DFT-based identification of subsynchronous oscillation parameters using synchrophasor data," *IEEE Trans. Smart Grid*, vol. 11, no. 3, pp. 2662–2675, 2020.

[15] T. Rauhala, A. M. Gole, and P. Järventausta, "Detection of subsynchronous torsional oscillation frequencies using phasor measurement," *IEEE Trans. Power Del.*, vol. 31, no. 1, pp. 11–19, 2016.

[16] F. Zhang, L. Cheng, W. Gao, and R. Huang, "Synchrophasors-based identification for subsynchronous oscillations in power systems," *IEEE Trans. Smart Grid*, vol. 10, no. 2, 2019.

[17] X. Yang, L. Yang, X. Xiao, and Y. Wang, "A novel detection method for supersynchronous resonance from synchrophasor data," *IEEE Trans. Power Syst.*, pp. 1–13, 2022.

[18] F. Zhang *et al.*, "An improved interpolated DFT-based parameter identification for sub-/super-synchronous oscillations with synchrophasors," *IEEE Trans. Power Syst.*, vol. 38, no. 2, pp. 1714–1727, 2023.

[19] A. Messina and V. Vittal, "Nonlinear, non-stationary analysis of interarea oscillations via Hilbert spectral analysis," *IEEE Trans. Power Syst.*, vol. 21, no. 3, pp. 1234–1241, 2006.

[20] P. G. Estevez, P. Marchi, C. Galarza, and M. Elizondo, "Non-stationary power system forced oscillation analysis using synchrosqueezing transform," *IEEE Trans. Power Syst.*, vol. 36, no. 2, pp. 1583–1593, 2021.

[21] Y. Ma *et al.*, "Subsynchronous oscillation analysis using multisynchrosqueezing transform and dissipating energy flow method," *IEEE Trans. Ind. Appl.*, vol. 58, no. 3, pp. 3134–3141, 2022.

[22] P. G. Estevez, P. Marchi, F. Messina, and C. Galarza, "Forced oscillation identification and filtering from multi-channel time-frequency representation," *IEEE Trans. Power Syst.*, vol. 38, no. 2, pp. 1257–1269, 2023.

[23] J. Follum, J. Holzer, and P. Etingov, "A statistics-based threshold for the rms-energy oscillation detector," *International Journal of Electrical Power Energy Systems*, vol. 128, p. 106685, 2021.

[24] S. Maslennikov, B. Wang, and E. Litvinov, "Dissipating energy flow method for locating the source of sustained oscillations," *International Journal of Electrical Power Energy Systems*, vol. 88, pp. 55–62, 2017.

[25] R. B. Myers and D. J. Trudnowski, "Effects of forced oscillations on spectral-based mode-shape estimation," in *2013 IEEE Power Energy Society General Meeting*, 2013, pp. 1–6.

[26] M. Donnelly, D. Trudnowski, J. Colwell, J. Pierre, and L. Dosiek, "Rms-energy filter design for real-time oscillation detection," in *2015 IEEE Power Energy Society General Meeting*, 2015, pp. 1–5.

[27] X. Xie, Y. Zhan, J. Shair, Z. Ka, and X. Chang, "Identifying the source of subsynchronous control interaction via wide-area monitoring of sub/super-synchronous power flows," *IEEE Trans. Power Del.*, vol. 35, pp. 2177–2185, 2020.

[28] P. G. Estevez, P. Marchi, C. Galarza, and M. Elizondo, "Complex dissipating energy flow method for forced oscillation source location," *IEEE Trans. Power Syst.*, vol. 37, no. 5, pp. 4141–4144, 2022.

[29] R. Arghandeh *et al.*, "Synchrophasor monitoring for distribution systems: Technical foundations and application," NASPI, Tech. Rep., 2018.

[30] M. Izadi and H. Mohsenian-Rad, "Event location identification in distribution networks using waveform measurement units," in *2020 IEEE PES Innovative Smart Grid Technologies Europe*, 2020, pp. 924–928.

[31] G. Yu, M. Yu, and C. Xu, "Synchroextracting transform," *IEEE Trans. Ind. Electron.*, vol. 64, no. 10, pp. 8042–8054, 2017.

[32] G. Thakur and H.-T. Wu, "Synchrosqueezing-based recovery of instantaneous frequency from nonuniform samples," *SIAM Journal on Mathematical Analysis*, vol. 43, no. 5, pp. 2078–2095, 2011.

[33] S. Chen, S. Wang, B. An, R. Yan, and X. Chen, "Instantaneous frequency band and synchrosqueezing in time-frequency analysis," *IEEE Trans. Signal Process.*, vol. 71, pp. 539–554, 2023.

[34] R. Behera, S. Meignen, and T. Oberlin, "Theoretical analysis of the second-order synchrosqueezing transform," *Applied and Computational Harmonic Analysis*, vol. 45, no. 2, pp. 379–404, 2018.

[35] Y. Cheng *et al.*, "Real-world subsynchronous oscillation events in power grids with high penetrations of inverter-based resources," *IEEE Trans. Power Syst.*, vol. 38, no. 1, pp. 316–330, 2023.

[36] W. Liu, X. Xie, J. Shair, and X. Li, "A nearly decoupled admittance model for grid-tied VSCs under variable operating conditions," *IEEE Trans. Power Electron.*, vol. 35, no. 9, pp. 9380–9389, 2020.

[37] F. Zhang, "Simulated synchrophasors in SSOs and phasor measurement data recorded during a subsynchronous oscillation incident in an actual power system," 2021.

[38] B. Gao, Y. Wang, W. Xu, and G. Yang, "Identifying and ranking sources of SSR based on the concept of subsynchronous power," *IEEE Trans. Power Del.*, vol. 35, no. 1, pp. 258–268, 2020.

[39] Y. Li, L. Fan, and Z. Miao, "Replicating real-world wind farm SSR events," *IEEE Trans. Power Del.*, vol. 35, no. 1, pp. 339–348, 2020.

[40] "Rio grade valley projects," *Electric Transmission Texas, Austin, TX, USA*, 2016.

Taimur Zaman recieved his B.Sc degree in electrical power from COMSATS University, Islamabad, Pakistan in 2015 and M.Sc degree in power and control engineering from CECOS University, Peshawar, Pakistan, in 2019. He is pursuing Ph.D in electronics and electrical engineering at the University of Strathclyde, Glasgow, UK. His research area is focused on power system disturbance identification, resiliency & control. Before he started his PhD in June 2021, he worked as R&D engineer facilitating development projects related to power systems and control. He has also been working as a research assistant at CECOS University of Science and Technology, Pakistan, from 2017-2019.

Mazheruddin Syed (Senior Member, IEEE) received the B.E. degree in electrical and electronics engineering from Osmania University, Hyderabad, India, in 2011, the M.Sc. degree in electrical power engineering from the Masdar Institute of Science and Technology, Abu Dhabi, UAE, in 2013, and the Ph.D. degree in electrical power systems from the University of Strathclyde, Glasgow, Scotland, in 2018.,He is currently the Power Systems Lead for Scotland at WSP, U.K., working on innovation projects with transmission and distribution system operators. Before joining WSP, he was a Strathclyde Chancellor's Fellow (Lecturer/Assistant Professor) with the Department for Electronic and Electrical Engineering, University of Strathclyde, Glasgow, and was the Manager of the Dynamic Power Systems Laboratory. Prior to his position as a Chancellor's Fellow, he was a Research Fellow with the Institute for Energy and Environment, University of Strathclyde. He has contributed to innovative power system research projects with a strong publication record of more than 70 peer-reviewed papers in top-tier journals and conferences. His research interests include decentralized and distributed control, real-time controller and power hardware in the loop simulations, and systems level validations.,Dr. Syed is active in a number of national and international committees. He is the Technical Committee Secretary of IEEE PES Task Force on Cloud-Based Control and Co-Simulation of Multi-Party Resources.

Zhiwang Feng (Member, IEEE) received the B.Eng. degree in electronic and electrical engineering from North China Electric Power University, Baoding, China, in 2017, the M.Sc. degree in electronic and electrical engineering from the University of Manchester, Manchester, U.K., in 2018, and the Ph.D. degree in electronic and electrical engineering from the University of Strathclyde, Glasgow, U.K., in 2023. He is currently a Research Associate, leading the microgrid and power hardware-in-the-loop experimental validation with the Dynamic Power Systems Laboratory, Institute for Energy and Environment, University of Strathclyde. His research interests include power system disturbance identification and mitigation, geographically distributed real-time simulation, real-time power hardware-in-the-loop simulation, and their applications to the experimental validation of power converters, microgrid control, and electric power systems.

Graeme Burt (Member, IEEE) received the B.Eng. degree in electrical and electronic engineering and the Ph.D. degree in fault diagnostics in power system networks from the University of Strathclyde, Glasgow, U.K., in 1988 and 1992, respectively. He is currently a Distinguished Professor of electrical power systems with the University of Strathclyde where he directs the Institute for Energy and Environment, directs the Rolls-Royce University Technology Centre in Electrical Power Systems, and is Lead Academic for the Power Networks Demonstration Centre (PNDC). In addition, he serves on the board of DERlab e.V., the association of distributed energy laboratories. His research interests include the areas of decentralized energy and smart grid protection and control, electrification of aerospace and marine propulsion, dc and hybrid power distribution, and experimental systems testing and validation with power hardware in the loop.